Intermittency of an incompressible passive vector convected by isotropic turbulence

Jingyuan Yang[*] and Toshiyuki Gotoh[†]
Department of Physical Science and Engineering, Nagoya Institute of Technology, Gokiso, Nagoya 466-8555, Japan

Hideaki Miura[‡]
National Institute for Fusion Science, Oroshi, Toki City, Gifu, Japan

Takeshi Watanabe[§]
Department of Physical Science and Engineering, Nagoya Institute of Technology, Gokiso, Nagoya 466-8555, Japan

(Received 15 May 2019; published 6 November 2019)

The intermittency of an incompressible passive vector convected by homogeneous isotropic turbulence is studied by comparison with that of the velocity and passive scalar. This is used to explore the physics underlying the differences in statistical properties between the velocity vector and passive scalar. Direct numerical simulations with grid points of 1024^3 and two types of forcing method are performed at Reynolds numbers of $\mathrm{Re}_\lambda \sim 200$, 300, and 400. It is found that the probability density function (PDF) of the passive vector is wider than Gaussian. The PDFs of the logarithm of the dissipation rates of the kinetic energy, for the velocity and passive vector, are close to each other and well approximated by the log-normal distribution. Unlike the pressure PDF, which is negatively skewed, the PDF for the pseudopressure $P(q)$ is nearly symmetric. Visualization results show that the pseudoenstrophy Ω_w for the passive vector is close to sheetlike, similar to the case of the passive scalar, while the enstrophy is tubelike. The scaling exponents of the passive vector moments are found to be anomalous, nonuniversal at high order, and intermediate between the velocity and passive scalar for the order $p \geqslant 4$. The pseudopressure tends to reduce the extreme events, while the linearity of the fundamental equation leads to stronger intermittency.

DOI: 10.1103/PhysRevFluids.4.114602

I. INTRODUCTION

Scalar transport and mixing by turbulent flow are among the central problems in fundamental research on turbulence. The equation of a passive scalar shares common features with the Navier-Stokes equation, such as convection by turbulent velocity and dissipation (smearing) by molecular diffusivity, but lacks a pressure term. These properties simplify the problem in that the equation is for one component and is linear and local in space; this is unlike the Navier-Stokes equation, which is for three components and is nonlinear and nonlocal in space. Therefore, it is reasonable to assume that mathematical and physical analysis of the statistical properties of scalar fluctuations could be

[*]cjv13503@stn.nitech.ac.jp
[†]gotoh.toshiyuki@nitech.ac.jp
[‡]miura.hideaki@nifs.ac.jp
[§]watanabe.takeshi@nitech.ac.jp

simpler than analyzing turbulent velocity fluctuations. Indeed, following Kolmogorov's theory [1], fundamental theories have been developed by Obukhov-Corrsin [2–4], Batchelor [5], Batchelor, Howells, and Townsend [6], and many other researchers. Early studies are mostly concerned with low-order statistics, such as scalar transport flux and the scalar spectrum. Subsequently, the issue of intermittency has arisen in the fundamental study of turbulence [7,8].

A large number of studies on intermittency have been conducted, concerning both velocity and scalar fluctuations [8–10]. One of the central quantities of interest in intermittency studies is the scaling exponents of the moments of the velocity and scalar increments, which are assumed to obey the power law in the inertial convective range [8]. It is now widely recognized that the exponents of the passive scalar at high order are smaller than those of the velocity and tend to saturate, meaning that the passive scalar is more intermittent than the velocity field [10–15].

Kraichnan proposed a model for the passive scalar, known as the Kraichnan model [16,17]. In the model, the velocity field is assumed to follow a Gaussian distribution with the delta correlation in time (Kraichnan velocity ensemble). The most distinctive aspect of the model is that the scaling exponents for the moments of the scalar increments are derived analytically. A novel and important aspect is the fact that the scaling exponents are determined by the zero mode (homogeneous solution) of the linear operator for the scalar moments, and are thus universal [18]. The model has been extended to many other problems, such as the passive magnetic field [19], passive scalars in the inverse-cascading range for incompressible [20,21] and compressible Kraichnan velocity ensembles [22], and finitely correlated Gaussian velocity ensembles [23]. It is argued that when the velocity field is (nearly) Gaussian, analysis in terms of the zero mode of the linear operator is effective and the universality of the scaling exponents for the passive scalar moments applies.

However, the turbulent velocity field in three dimensions obeying the Navier-Stokes equation differs significantly from the Kraichnan velocity ensemble, being neither Gaussian nor white noise, and the energy is forward cascading. Indeed, Gotoh and Watanabe [24] studied the intermittency of two passive scalars in three dimensions that are convected by the same turbulent velocity field of the Navier-Stokes equation, but are excited by different mechanisms, one being the uniform mean gradient and the other being Gaussian random injection that is white in time. It has been found that the scaling exponents of the moments of the scalar increments differ at large scales and are thus not universal [24], suggesting that our understanding of universality and intermittency is insufficient.

In addition to the intrinsic properties of passive scalar intermittency, it is also important to consider the physics underlying statistical differences between the velocity and passive scalar. One method to explore is to introduce an equation that shares as many common properties and structure as both of the Navier-Stokes and passive scalar equations, and to study its statistical properties. We have previously studied fundamental statistical properties, i.e., low-order statistical properties of the spectra and transfer fluxes of an incompressible passive vector convected by isotropic turbulence [25].

The passive vector is assumed to obey

$$\left(\frac{\partial}{\partial t}+\boldsymbol{u}\cdot\nabla\right)\boldsymbol{w}=-\nabla q+\alpha\nabla^2\boldsymbol{w},\quad \nabla\cdot\boldsymbol{w}=0, \tag{1}$$

where the pseudopressure q is introduced to ensure incompressibility of the vector $\boldsymbol{w}$ and α is the pseudoviscosity [25–32]. The commonalities between Eq. (1) and the Navier-Stokes equation are as follows: (1) three components in $\boldsymbol{w}$, (2) the convection by the velocity $\boldsymbol{u}$, (3) the pseudopressure q and incompressibility of $\boldsymbol{w}$, (4) the pseudoviscosity α, and (5) when α is absent, the total pseudoenergy $(1/2)\int \boldsymbol{w}^2 d\boldsymbol{x}$ is conserved. The presence of the pseudopressure introduces a nonlocal interaction into the dynamics of the passive vector $\boldsymbol{w}$. On the other hand, the difference is that the convective term is linear.

Compared to the passive scalar, the common properties of the equation of $\boldsymbol{w}$ are (1) the linearity of the convective term and (2) the molecular dissipation. Here, while three components of $\boldsymbol{w}$ are constrained through incompressibility, the passive scalar is free from constraints. Our expectation is that the above common properties and structure could make it easier to find the physical explanation for the differences and similarities in fluctuations of the velocity and passive scalar.

The findings in Ref. [25] are as follows:

(1) The statistical property of $\boldsymbol{w}$ is close to $\boldsymbol{u}$ at large scales and close to θ at small scales, at the Reynolds numbers investigated in the study.

(2) At large scales, the pseudopressure acts similarly to the pressure, but is less effective compared to the pressure at small scales.

(3) Therefore, the resemblance between $\boldsymbol{w}$ and $\boldsymbol{u}$ at large scales is due to the nonlocal effect arising from the pseudopressure, and the difference at small scales is due to the linearity of the convective term.

(4) When this interpretation is applied to the velocity, the difference in the properties of fluctuations between the velocity and passive scalar at small scales can ultimately be attributed to whether the convective term is nonlinear.

In other words, differences arise due to the nonlinear dynamics, and the kinematic constraints are of secondary importance. Since the above findings pertain only to low-order statistics, it is important to examine whether they also apply to the intermittency of the passive vector. In this paper, we examine the high-order statistics of three fields, in addition to the visualized field.

The paper is organized as follows. In Sec. II, the governing equations and the various statistical quantities are defined, and in Sec. III the numerical scheme and parameters are described. In Sec. IV, the results are presented, and a summary is given in Sec. V.

II. GOVERNING EQUATIONS

We consider three fields: the velocity field $\boldsymbol{u}$ for the incompressible turbulence, a solenoidal passively convected vector $\boldsymbol{w}$, and a passively convected scalar θ. These fields are assumed to be governed by the following equations:

$$\left(\frac{\partial}{\partial t}+\boldsymbol{u}\cdot\nabla\right)\boldsymbol{u}=-\nabla p+\nu\nabla^2\boldsymbol{u}+\boldsymbol{f}^u, \tag{2}$$

$$\nabla\cdot\boldsymbol{u}=0, \tag{3}$$

$$\left(\frac{\partial}{\partial t}+\boldsymbol{u}\cdot\nabla\right)\boldsymbol{w}=-\nabla q+\alpha\nabla^2\boldsymbol{w}+\boldsymbol{f}^w, \tag{4}$$

$$\nabla\cdot\boldsymbol{w}=0, \tag{5}$$

$$\left(\frac{\partial}{\partial t}+\boldsymbol{u}\cdot\nabla\right)\theta=\kappa\nabla^2\theta+f^\theta, \tag{6}$$

where $p(\boldsymbol{x},t)$ is the pressure, ν denotes the kinetic viscosity, and κ is the diffusive coefficient for θ. The last terms on the right-hand side, $\boldsymbol{f}^u(\boldsymbol{x},t)$, $\boldsymbol{f}^w(\boldsymbol{x},t)$, and $f^\theta(\boldsymbol{x},t)$, are external forcings for the vectors and the scalar injection; their statistical properties are described later. The vorticity, pseudovorticity, and scalar gradient are defined as

$$\boldsymbol{\omega}=\nabla\times\boldsymbol{u},\quad \boldsymbol{\zeta}=\nabla\times\boldsymbol{w},\quad \boldsymbol{g}=\nabla\theta, \tag{7}$$

respectively.

We assume in this study that all three fields are in a statistically steady state and are homogeneous and isotropic. Therefore, the mean values of the kinetic energy, the pseudokinetic energy, and the scalar variance per unit mass and their corresponding spectra are defined by

$$E_u=\frac{1}{2}\langle\boldsymbol{u}^2(\boldsymbol{x},t)\rangle=\frac{3}{2}u_{\rm rms}^2=\int_0^\infty E_u(k)dk, \tag{8}$$

$$E_w=\frac{1}{2}\langle\boldsymbol{w}^2(\boldsymbol{x},t)\rangle=\frac{3}{2}w_{\rm rms}^2=\int_0^\infty E_w(k)dk, \tag{9}$$

$$E_\theta=\frac{1}{2}\langle\theta^2(\boldsymbol{x},t)\rangle=\frac{1}{2}\theta_{\rm rms}^2=\int_0^\infty E_\theta(k)dk, \tag{10}$$

respectively, where $\langle\ \rangle$ denotes the ensemble average. The mean dissipation rates of the kinetic energy and the pseudokinetic energy, and the destruction rate of the passive scalar variance per unit mass (hereafter referred to as dissipation rates), are defined as

$$\bar{\epsilon}_u = \langle \epsilon_u(\boldsymbol{x}, t) \rangle = \nu \langle (\nabla \boldsymbol{u})^2 \rangle, \tag{11}$$

$$\bar{\epsilon}_w = \langle \epsilon_w(\boldsymbol{x}, t) \rangle = \alpha \langle (\nabla \boldsymbol{w})^2 \rangle, \tag{12}$$

$$\bar{\epsilon}_\theta = \langle \epsilon_\theta(\boldsymbol{x}, t) \rangle = \kappa \langle (\nabla \theta)^2 \rangle, \tag{13}$$

respectively. Throughout this study the Schmidt numbers $\mathrm{Sc}_w = \nu/\alpha$, $\mathrm{Sc}_\theta = \nu/\kappa$ are set to unity to make the dissipation length the same. The fundamental turbulence parameters, such as the integral length L_u, the Taylor micro-scale length λ, the Kolmogorov length η, the Taylor micro-scale Reynolds number Re_λ, the large eddy turn-over time $T_e = L_u/u_{\mathrm{rms}}$, and the time duration for time average T_{av}, are defined in the standard way and as described in Ref. [25].

III. NUMERICAL SIMULATIONS

The numerical simulation method is the same as in Refs. [25,33], and the majority of the computation was carried out on a plasma simulator (FX100, Fujitsu) at the Toki site of the National Institute for Fusion Science, Japan. Two kinds of random forcing and scalar injection (hereafter referred to as forcing) were employed to see the effects of large-scale properties on the small-scale statistics. The first type of forcing is Gaussian random forcing, which is white in time, has spectral support at low wavenumbers, and is used for runs A–C:

$$\left\langle f_i^A(\boldsymbol{k}, t) f_j^A(-\boldsymbol{k}, s) \right\rangle = \frac{1}{2} \frac{F_0(k)}{2\pi k^2} P_{ij}(\boldsymbol{k}) \delta(t - s), \tag{14}$$

$$\langle f^\theta(\boldsymbol{k}, t) f^\theta(-\boldsymbol{k}, s) \rangle = \frac{F_0(k)}{2\pi k^2} \delta(t - s), \tag{15}$$

$$F_0(k) = \begin{cases} \frac{\epsilon_{\mathrm{inj}}^B}{k_{f\max} - k_{f\min}} & \text{for } k_{f\min} \leqslant |\boldsymbol{k}| < k_{f\max} \\ 0 & \text{otherwise.} \end{cases} \tag{16}$$

The second type of forcing is linearly proportional to the field at low-k band and is applied to run D:

$$\boldsymbol{f}^A(\boldsymbol{k}, t) = c_A(t) G(k) \boldsymbol{A}(\boldsymbol{k}, t), \tag{17}$$

$$f^\theta(\boldsymbol{k}, t) = c_\theta(t) G(k) \theta(\boldsymbol{k}, t), \tag{18}$$

$$G(k) = \begin{cases} 1 & \text{for } k_{f\min} \leqslant k < k_{f\max} \\ 0 & \text{otherwise,} \end{cases} \tag{19}$$

$$c_A(t) = \frac{\epsilon_{\mathrm{inj}}^A}{\int G(k) E_A(k, t) dk}, \tag{20}$$

where $\boldsymbol{A}$ denotes $\boldsymbol{u}$ or $\boldsymbol{w}$, respectively, and A stands for u, w, or θ, respectively. The initial fields are chosen to be Gaussian random variables in $\boldsymbol{k}$-space with spectrum

$$E_A(k, t = 0) = N_A k_0^{-5} k^4 e^{-2(k/k_0)^2}, \tag{21}$$

TABLE I. Direct numerical simulation parameters and characteristic statistics. C_K^u, C_K^w, and C_{OC}^θ are Kolmogorov and Obukhov-Cossin constants, respectively. See Eqs. (25)–(27).

	Run A	Run B	Run C	Run D
N	1024	1024	1024	1024
Re_λ	194.2	300.9	397.1	300.9
$k_{\max}\eta$	2.25	1.14	0.80	1.22
$[k_{f_{\mathrm{low}}}, k_{f_{\mathrm{high}}}]$	[2,3]	[2,3]	[2,3]	[2,3]
Δt	2×10^{-4}	10^{-4}	5×10^{-5}	10^{-4}
ν	5×10^{-4}	2×10^{-4}	1.2×10^{-4}	2×10^{-4}
T_e	0.79	0.79	0.82	0.88
T_{av}/T_e	11.16	10.58	10.29	10.02
$\bar{E}_u$	0.98	0.94	0.91	0.82
$\bar{E}_w$	0.61	0.60	0.67	0.60
$\bar{E}_\theta$	0.15	0.15	0.15	0.13
$\varepsilon_{\mathrm{inj}}^u$	0.3	0.3	0.3	0.3
$\varepsilon_{\mathrm{inj}}^w$	0.3	0.3	0.3	0.3
$\varepsilon_{\mathrm{inj}}^\theta$	0.1	0.1	0.1	0.1
$\bar{\epsilon}_u$	0.34	0.32	0.29	0.25
$\bar{\epsilon}_w$	0.32	0.30	0.33	0.26
$\bar{\epsilon}_\theta$	0.10	0.10	0.10	0.09
L_u	0.64	0.62	0.64	0.65
L_w	0.65	0.65	0.64	0.67
L_θ	0.43	0.44	0.43	0.42
λ_u	0.120	0.076	0.061	0.081
λ_w	0.097	0.063	0.050	0.068
λ_θ	0.055	0.035	0.027	0.035
C_K^u	1.57	1.55	1.57	1.59
C_K^w	0.93	1.00	1.00	1.06
C_{OC}^θ	0.65	0.69	0.68	0.69

where N_A is the normalization constant to set the initial (pseudo)energy to be 3/2 or the variance to be unity. Each run is started from the Gaussian random initial field with low Reynolds number on the small number of grid points of 256^3, and integrated until a statistically steady state is attained. The decision whether or not the steady state is achieved is made by observing that the energy spectra do not change in time and that the evolution of the energy dissipation rates stays around the energy injection rates. Then the Reynolds numbers and the number of grid points are increased to 512^3, and the same process is repeated to attain steady state on the 1024^3 grid points. It takes longer time to become stationary for higher Reynolds number, i.e., for run C, over $5T_e$ is required, and all the data in the transient period of runs are not taken into account to determine the statistical properties of the flow.

The averages are taken as the volume average over the domain and/or the time average only at steady state. Their mean values at steady state are listed in Table I. It is argued that the spatial resolution in direct numerical simulation (DNS) requires $k_{\max}\bar{\eta} > 1.5$ for the velocity but the resolution for the passive scalar is more demanding because of the efficient transfer of the scalar variances to high wavenumbers and strong intermittency [13,25,34–36]. In particular the accurate computation of the extreme values or high-order moments of the scalar gradient requires large values of $k_{\max}\bar{\eta}_B$, say greater than 5 or more as reported in Refs. [34,35], where $\eta_B = \eta/\mathrm{Sc}^{1/2}$ is the Batchelor length. In the present DNSs $\eta_B = \eta$ because $\mathrm{Sc} = 1$, and the spatial resolution is $k_{\max}\bar{\eta} = 2.25$, 1.14, 0.80, and 1.22 for runs A, B, C, and D, respectively. Run A meets the requirement, and the spatial resolution of other runs is lower than the standard. However, in this

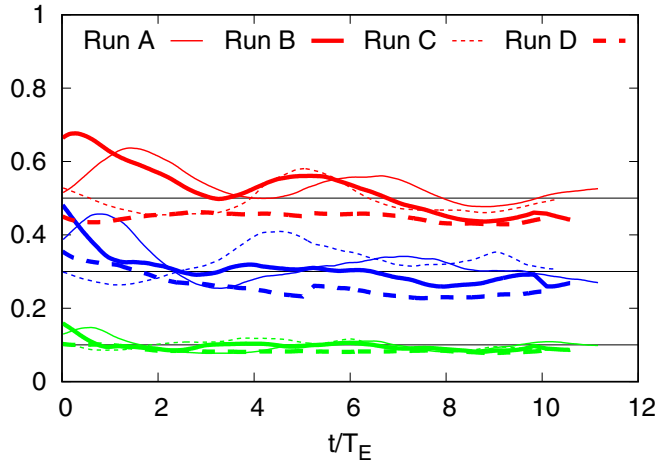

FIG. 1. Time variation of energy dissipation rates: red, $\epsilon_u(t)+0.2$; blue, $\epsilon_w(t)$; green, $\epsilon_\theta(t)$. Thin horizontal lines show the injection rates $\epsilon_{\rm inj}^A$ for $A = u, w, \theta$.

study, our concern is mostly on the statistical behavior in the inertial-convective range; therefore, we consider that as far as the scale of interests lies in the inertial-convective range the spatial resolution in the present DNS study does not affect the analysis. Indeed, it has been shown that the inertial range statistics are insensitive to the dissipation range [36].

IV. RESULTS

After examining the time evolution of the dissipation rates and three spectra, the intermittency of the three fields is studied by focusing mainly on three aspects: (1) the spatial geometry of the enstrophy, the pseudoenstrophy, and the square of the scalar gradient, (2) the probability density functions (PDFs), with a particular focus on their tails (related to extreme events), and (3) the scaling exponents of the moments of increments for various field variables as functions of the separation distance.

A. Evolution of energy dissipation rate and energy spectrum

The time variation of the dissipation rates after the initial transient period is shown in Fig. 1 (the origin of time means the initial time in steady state). For ease of visibility, the curves of $\epsilon_u(t)$ are shifted by 0.2. All dissipation rates for runs A, B, and C relax with oscillation to the injection rate with a period of about $6T_e$, while the dissipation rates for run D quickly reach steady-state values that are slightly smaller than the injection rates. The oscillation with a long period for the dissipation rates implies the need for a long time average to obtain well-converged statistics, especially for the high-order statistics. Indeed, the time average in this study is taken over a period longer than $10T_e$ (see Table I).

The mean spectra of the three fields can be normalized in terms of the Kolmogorov variables as

$$E_u^*(k\eta) = \bar{\epsilon}_u^{-1/4}\nu^{-5/4}E_u(k), \tag{22}$$

$$E_w^*(k\eta) = \bar{\epsilon}_w^{-1}\bar{\epsilon}_u^{3/4}\alpha^{-2}\nu^{3/4}E_w(k), \tag{23}$$

$$E_\theta^*(k\eta) = \bar{\epsilon}_\theta^{-1}\bar{\epsilon}_u^{3/4}\kappa^{-2}\nu^{3/4}E_\theta(k), \tag{24}$$

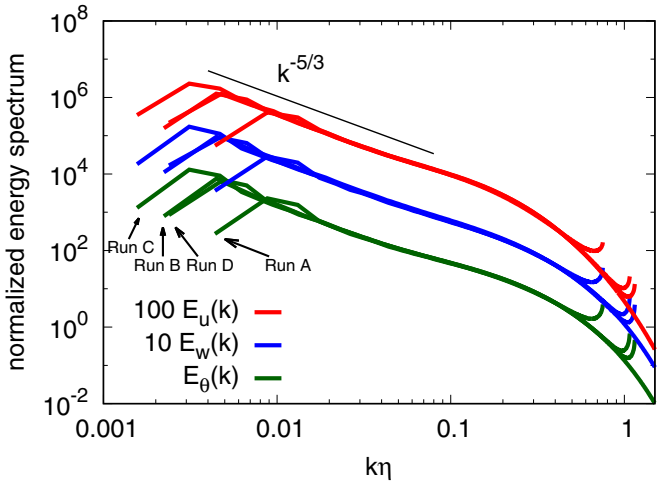

FIG. 2. Normalized mean spectra. The thin straight line indicates the $-5/3$ slope. For ease of visibility, curves of $E_u^*(k)$ and $E_w^*(k)$ are shifted by 100 and 10, respectively.

respectively, and shown in Fig. 2 [25]. For ease of visibility, the spectra $E_u(k)$ and $E_w(k)$ are multiplied by 100 and 10, respectively. The curves of the spectra for four runs collapse well onto a single curve, irrespective of the Reynolds number and forcing mechanism. The $-5/3$ power law for $E_u(k)$, $E_w(k)$, and $E_\theta(k)$ can be observed for $k\eta \in [0.01, 0.1]$. The nondimensional constants in the inertial-convective range are defined by

$$E_u(k) = C_K \bar{\epsilon}^{2/3} k^{-5/3}, \tag{25}$$

$$E_w(k) = C_K^w \bar{\epsilon}^{-1/3} \bar{\epsilon}_w k^{-5/3}, \tag{26}$$

$$E_\theta(k) = C_{OC} \bar{\epsilon}^{-1/3} \bar{\epsilon}_\theta k^{-5/3}, \tag{27}$$

and were found to be

$$C_K = 1.57, \quad C_K^w = 1.00, \quad C_{OC} = 0.68, \tag{28}$$

for run C. These values are consistent with those reported in the literature [9,10,13,24,25,33,37–39] and are insensitive to differences in the large-scale forcing mechanisms, suggesting the universality of these spectra at the inertial-convective range.

B. Visualization

Before studying intermittency in terms of the PDFs and scaling exponents, we present the visualization results of flow fields because it is useful to interpret the various properties of those statistics by relating them to the flow structure. Here, we examine the enstrophy, pseudoenstrophy, and square of the scalar gradient, defined as

$$\Omega_u(\boldsymbol{x}, t) = [\nabla \times \boldsymbol{u}]^2, \tag{29}$$

$$\Omega_w(\boldsymbol{x}, t) = [\nabla \times \boldsymbol{w}]^2, \tag{30}$$

$$\Omega_\theta(\boldsymbol{x}, t) = [\nabla \theta]^2, \tag{31}$$

respectively.

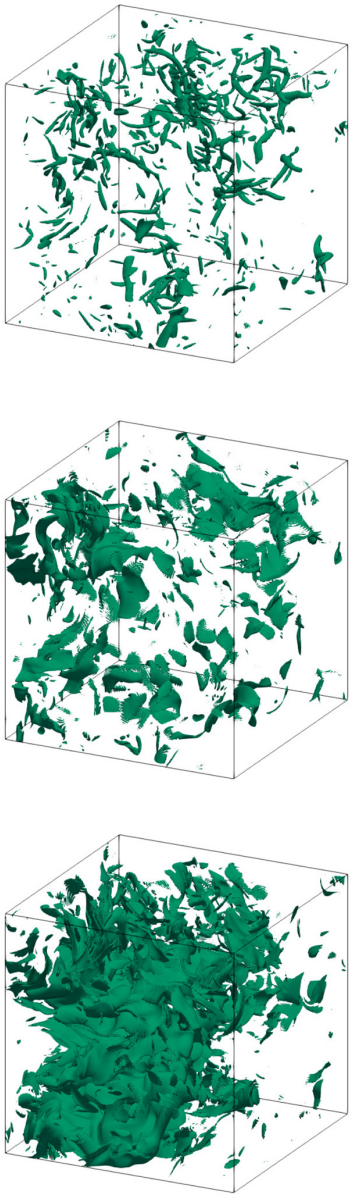

FIG. 3. Isosurface for Ω_u (top), Ω_w (middle), and Ω_θ (bottom) for run A with level of $8\langle\varepsilon_A\rangle/\nu$.

The isosurfaces of Ω_A (for $A = \omega, w, \theta$) at instantaneous time in the sub-box $x, y, z \in [0, L/4]$ for run A are shown in Fig. 3 with level $\Omega_A(\boldsymbol{x}, t) > 8\langle\Omega_A\rangle$. The geometry of the pseudovorticity for the passive vector is sheetlike. This is dissimilar to the tubelike geometry of the vorticity [40], but similar to the sheetlike geometry of the passive scalar gradient [41–43]. In the tubelike structure, the vortex lines are bundled in a circle, while in the sheetlike structure of the pseudovortex, the vortex lines are bundled into a sheet.

As we demonstrated in Ref. [25], the low-order statistics of the passive vector, such as the third-order structure function, energy spectrum, and flux, are close to those of the velocity field at large scales, while being close to those of the passive scalar at small scales. These findings are consistent

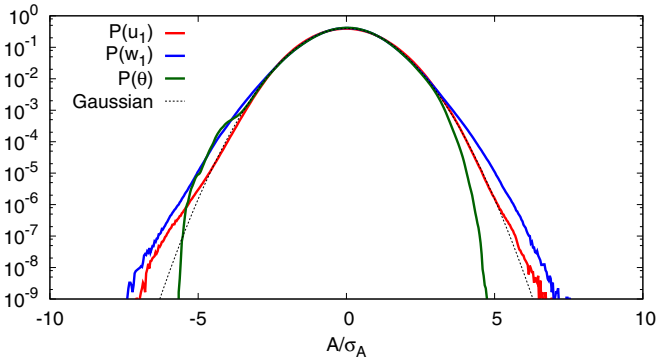

FIG. 4. Normalized probability density functions (PDFs) of u_1, w_1, and θ for run B. $A = u_1, w_1, \theta$ and σ_A denotes the standard deviation of A.

with the visualization, in that the sheetlike geometry of the passive vector is mostly attributed to the small-scale structure.

C. One-point probability density functions

Normalized one-point PDFs of u_1, w_1, θ for run B are shown in Fig. 4. Slight asymmetry of the PDFs is observed and we consider it is due to the finite length of the time average and to the forcing at low wave number band. The curve of $P(u_1)$ is close to a Gaussian distribution and $P(\theta)$ decays faster than the Gaussian on the right tail, which is consistent with the observation in Refs. [13,21,33]. However, there are also studies reporting the facts that the PDF of the passive scalar is Gaussian, exponential, or stretched exponential depending on conditions [44–47]. We also note that the PDF $P(w_1)$ is wider than the Gaussian at large amplitude. It is not known how this trend of $P(w_1)$ is generated, which is the subject of a future study.

The normalized PDFs $P(p)$ and $P(q)$ for run B are compared in Fig. 5. $P(p)$ is negatively skewed and has a long left tail, consistent with previous studies [48,49]. The left tail of $P(q)$ for run B is slightly longer than the right tail but the degree of the symmetry is stronger than that of $P(p)$. On the other hand, we observe that for runs A, C, and D the right tails of $P(q)$ are longer than the left tails (figures not shown). It is not known whether the asymmetry of $P(q)$ remains finite or vanishes when the time average is extended or whether it depends on the method of external injection.

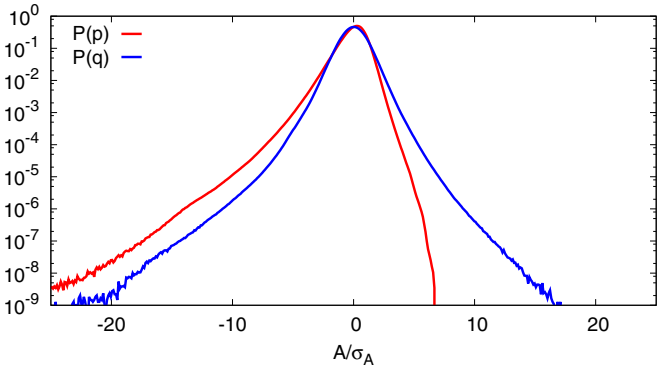

FIG. 5. Normalized PDFs of pressure p and pseudopressure q for run B. $A = p, q$.

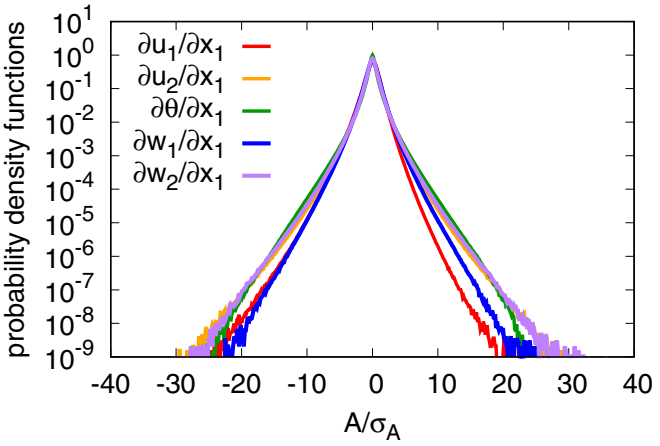

FIG. 6. Normalized PDFs of gradient fields ($\frac{\partial u_1}{\partial x_1}$, $\frac{\partial u_1}{\partial x_2}$, $\frac{\partial w_1}{\partial x_1}$, $\frac{\partial w_1}{\partial x_2}$, and $\frac{\partial \theta}{\partial x_1}$) for run A.

As seen in the top panel of Fig. 3, there are strong vortex tubes. For a fluid particle to rotate around the centerline of the thin tube, the pressure inside the tube must be much lower than the outside pressure; therefore, the longer left (negative) tail of $P(p)$ prevails. On the other hand, the domain of large Ω_θ is sheetlike. The sheetlike structure can be formed at the interface where two scalar blobs with a large difference in amplitude, of the order of $\theta_{\rm rms}$, meet under the convective motion of fluid [50]. As for Ω_w, the domain at large amplitude is roughly sheetlike. We infer from the sheetlike structure of the passive scalar that a $\boldsymbol{w}$ blob is passively compressed from both sides of the sheet under the convective motion of fluid. Since the pseudopressure gradient acts to keep a $\boldsymbol{w}$ blob incompressible, this can be achieved by q on one side of the sheet which is higher or lower than that on the other side. This is unlike the vortex tube.

The PDFs of the gradient fields for run A are compared in Fig. 6. The observations are as follows: (1) $P(\frac{\partial u_1}{\partial x_1})$ is negatively skewed, linked to energy transfer from large scales to smaller scales [33]. On the other hand, $P(\frac{\partial w_1}{\partial x_1})$ is symmetric and has a longer tail than that of $P(\frac{\partial u_1}{\partial x_1})$, and (2) the PDF tails of the transverse gradient of the velocity and passive vector are symmetric, very close to each other, and also close to $P(\frac{\partial \theta}{\partial x_1})$ up to moderate amplitudes.

The normalized PDFs of the gradients of pressure and pseudopressure $P(\frac{\partial p}{\partial x})$ and $P(\frac{\partial q}{\partial x})$ are shown in Fig. 7. The PDFs are symmetric and almost collapse onto each other [49,51].

The PDFs of $\log_{10}(\epsilon_A/\bar{\epsilon}_A)$ where $A = u, w, \theta$ are shown in Fig. 8. The PDFs of $\log_{10}(\epsilon_u/\bar{\epsilon}_u)$ and $\log_{10}(\epsilon_w/\bar{\epsilon}_w)$ collapse very well, and very close to the log-normal distribution [52]. On the other hand, the left tail of the PDF for $\log_{10}(\epsilon_\theta/\bar{\epsilon}_\theta)$ decays linearly with slope $n_\theta = 3/2$, which means that

$$P(\ln \epsilon_\theta) d \ln \epsilon_\theta \propto \exp(n_\theta |\ln(\epsilon_\theta/\bar{\epsilon}_\theta)|) d \ln \epsilon_\theta \propto (\epsilon_\theta)^{n_\theta - 1} d\epsilon_\theta, \tag{32}$$

so that

$$P(\epsilon_\theta) \propto \epsilon_\theta^{1/2}, \tag{33}$$

for small ϵ_θ. The left tails of $P(\log_{10}(\epsilon_u/\bar{\epsilon}_u))$ and $P(\log_{10}(\epsilon_w/\bar{\epsilon}_w))$ look to have slope $n_u = n_w = 4$. The above behavior is also observed in runs B, C, and D, and the exponent $n_\theta = 3/2$ is unchanged.

Yeung *et al.* [53] studied the PDFs for $x = \epsilon/(\nu\Omega)$, the ratio of the kinetic energy dissipation rate to the enstrophy, and found that the PDF tails obey the power law as $P(x) \propto x^{3/2}$ and $x^{-5/2}$ for small and large x, respectively. The essence of the argument is that the weak dissipation or weak

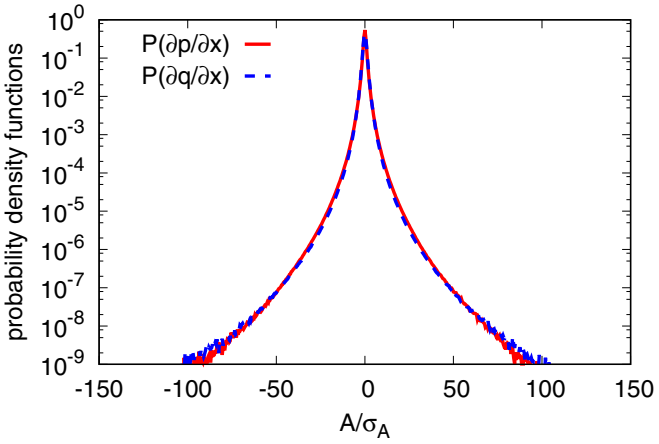

FIG. 7. Normalized PDFs of gradient of pressure and pseudopressure ($\frac{\partial p}{\partial x_1}$ and $\frac{\partial q}{\partial x_1}$) for run A.

enstrophy corresponds to the nearly Gaussian velocity field and obeys the chi-square distribution

$$\chi_k(z) = \frac{1}{\Gamma\left(\frac{k}{2}\right)} z^{k/2-1} e^{-z/2} \tag{34}$$

with the degree of freedom k, where Γ is the gamma function. If the same argument is applied to the scalar destruction rate ϵ_θ, we obtain $\chi_3(\epsilon_\theta) \propto \epsilon_\theta^{1/2}$ with $k = 3$ because ϵ_θ is the sum of three squared terms, which agrees well with Eq. (33). On the other hand, the dissipation rate is computed as $\epsilon_u = \nu(\partial u_i/\partial x_j)^2$ (and the same formula for ϵ_w) so that the number of terms is counted as eight under the incompressibility condition. Then we have $\chi_8(\epsilon_A) \propto \epsilon_A^3$ with $k = 8$ in agreement with $n_A - 1 = 3$ for $n_A = 4$, where $A = u$ or w. Instead, if we compute the dissipation rate by $\epsilon_u^s = (\nu/2)(\partial u_i/\partial x_j + \partial u_j/\partial x_i)^2$ under the incompressibility condition we have five terms so that $k = 5$ and $n_A = k/2 = 5/2$. Indeed we confirmed by the additional DNS that the left tail of $P(\beta_A^s)$, where $\beta_A^s = \log_{10}(\epsilon_A^s/\bar{\epsilon}_A^s)$, has the slope of 5/2 while the right tail collapses almost on $P(\beta_A)$ (figure not

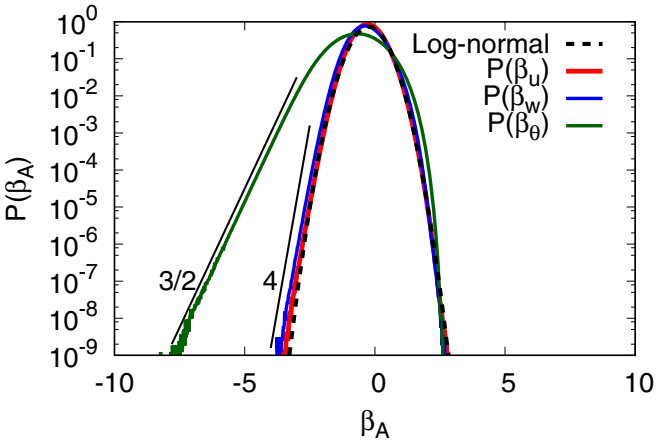

FIG. 8. PDFs of $\beta_u = \log_{10}(\epsilon_u/\bar{\epsilon}_u)$ (red), $\beta_w = \log_{10}(\epsilon_w/\bar{\epsilon}_w)$ (blue), and $\beta_\theta = \log_{10}(\epsilon_\theta/\bar{\epsilon}_\theta)$ (green) for run A. Thin black line shows the log-normal distribution and the straight line shows slope 3/2, respectively.

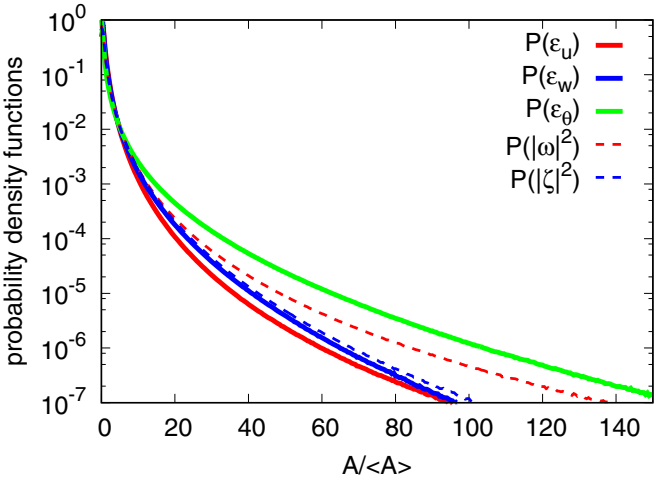

FIG. 9. PDFs of ϵ_u, ϵ_w, ϵ_θ, $\boldsymbol{\omega}^2$, and $\boldsymbol{\zeta}^2$ for run A.

shown) in the similar plot to Fig. 8. This suggests that for weak amplitudes of the dissipations the statistics dominates the dynamics.

The PDFs as functions of $\epsilon_A/\bar{\epsilon}_A$ for $A = u, w, \theta$ are plotted in Fig. 9. They are also compared with the PDFs of the enstrophy and pseudoenstrophy. The PDF tail of $\boldsymbol{\omega}^2$ is longer than that of the PDF of ϵ_u at the Reynolds number studied, which is consistent with the results of Ref. [54]. The same trend is observed in the comparison of $P(\epsilon_w)$ and $P(\boldsymbol{\zeta}^2)$, but the difference between the two curves is smaller.

D. Two-point probability density functions

Figure 10 shows the two-point PDFs for $\delta_r u_L = u(\boldsymbol{x} + r\boldsymbol{e}_x) - u(\boldsymbol{x})$, $\delta_r u_T$, $\delta_r w_L$, $\delta_r w_T$, and $\delta_r \theta$ for $r = n\Delta x$ for $n = 4$, 16, and 64, where L and T denote the longitudinal and transverse components of $\delta\boldsymbol{v}$ and $\delta\boldsymbol{w}$, respectively. Similarly, the PDFs of the increments of the pressure and pseudopressure are shown in Fig. 11. As reported in the literature, the PDFs become wider as the separation distance decreases and their tails change from convex to concave [13,33]. The PDF tails at large amplitudes, as a measure of the wideness of the PDF, are on the order of $P(\delta u_L)$, $P(\delta w_L)$, and $P(\delta u_T) \sim P(\delta w_T)$ for all separation distances studied. $P(\delta q)$ and $P(\delta p)$ are symmetric and close to each other at a small separation distance, but $P(\delta q)$ becomes slightly narrower than $P(\delta p)$ as the separation distance increases.

E. Scaling exponents of increment moments

The way that the increment moments change as a function of the separation distance provides information on how the fluctuation intensity changes with scales. It is expected that, in the inertial range, they obey the power law. The moments examined here are

$$S_p^{uL}(r) = \langle |\delta u_L(r)|^p \rangle \propto r^{\xi_p^{uL}}, \tag{35}$$

$$S_p^{uT}(r) = \langle |\delta u_T(r)|^p \rangle \propto r^{\xi_p^{uT}}, \tag{36}$$

$$S_p^{wL}(r) = \langle |\delta w_L(r)|^p \rangle \propto r^{\xi_p^{wL}}, \tag{37}$$

$$S_p^{wT}(r) = \langle |\delta w_T(r)|^p \rangle \propto r^{\xi_p^{wT}}, \tag{38}$$

$$S_p^{\theta}(r) = \langle |\delta \theta(r)|^p \rangle \propto r^{\xi_p^{\theta}}, \tag{39}$$

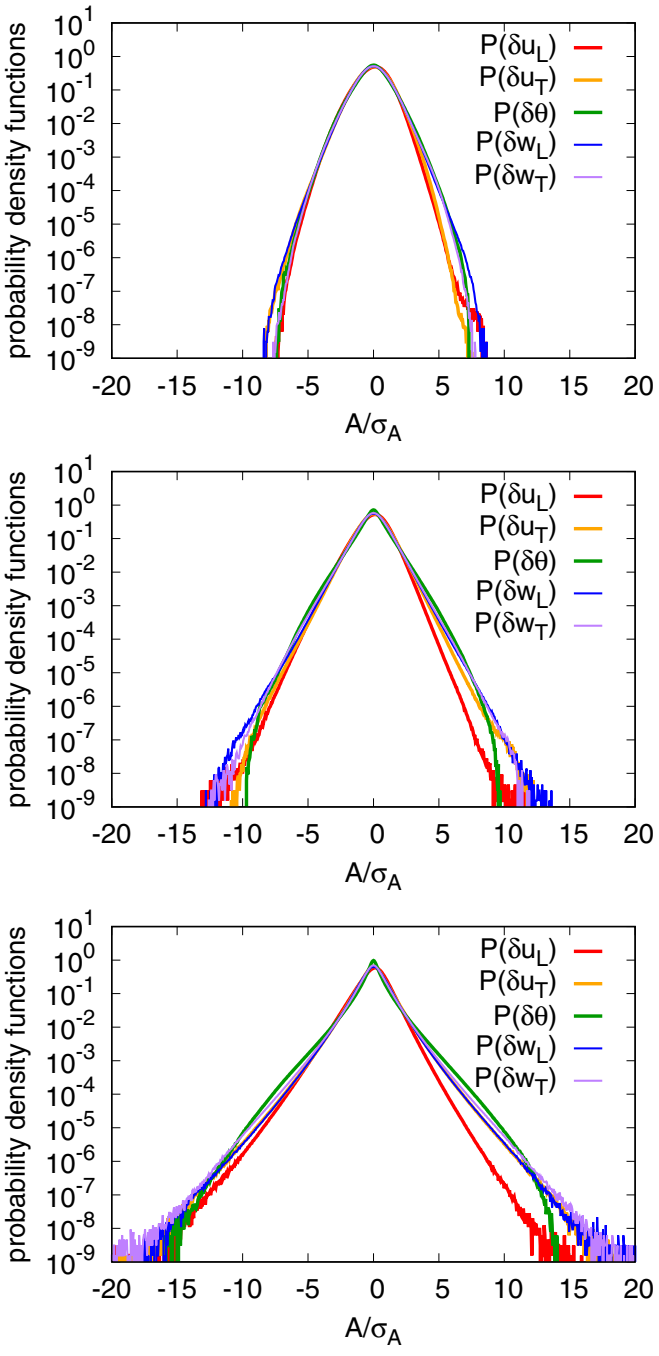

FIG. 10. Normalized PDFs of increments $\delta_r u_L$, $\delta_r u_T$, $\delta_r w_L$, $\delta_r w_T$, and $\delta_r \theta$ for run B. Top, $r = 64\Delta x$; middle, $r = 16\Delta x$, $r = 4\Delta x$.

where $\delta u_L = (\boldsymbol{u}(\boldsymbol{x}+\boldsymbol{r}) - \boldsymbol{u}(\boldsymbol{x})) \cdot \frac{\boldsymbol{r}}{r}$ denotes the component of $\delta\boldsymbol{u}(\boldsymbol{r})$ parallel to the separation vector $\boldsymbol{r}$, and δu_T is one of the components of $\delta\boldsymbol{u}$ perpendicular to $\boldsymbol{r}$, and similarly for δw_T.

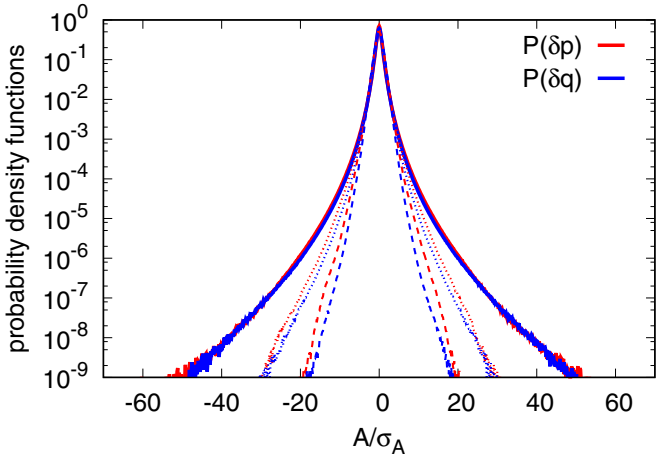

FIG. 11. Normalized PDFs of $\delta_r p$ and $\delta_r q$ for run B for $r = 4\Delta x$ (solid lines), $16\Delta x$ (dotted lines), and $64\Delta x$ (dashed lines).

The transfer fluxes of the (pseudo)kinetic energy and the scalar variance are defined in terms of the filtered variables, for example, as the product of the rate of strain tensor and the Reynolds stress with filter width Δ, which requires a large number of computations. To avoid this, in this study, we consider the moments as surrogates of the transfer fluxes of the (pseudo)kinetic energy and the scalar variance,

$$r^{p/3}\Pi^u_{p/3}(r) = Q^u_p(r) = \langle|\delta u_L(r)[\delta \boldsymbol{u}(r)]^2|^{p/3}\rangle \propto r^{\mu^u_p}, \tag{40}$$

$$r^{p/3}\Pi^w_{p/3}(r) = Q^w_p(r) = \langle|\delta u_L(r)[\delta \boldsymbol{w}(r)]^2|^{p/3}\rangle \propto r^{\mu^w_p}, \tag{41}$$

$$r^{p/3}\Pi^\theta_{p/3}(r) = Q^\theta_p(r) = \langle|\delta u_L(r)[\delta \theta(r)]^2|^{p/3}\rangle \propto r^{\mu^\theta_p}, \tag{42}$$

respectively. As far as the scaling arguments are concerned, the above moments are expected to provide equivalent knowledge of the scaling behavior of the transfer fluxes.

To evaluate how the scaling behavior varies with respect to the separation distance, we examine their logarithmic derivatives:

$$\xi^A_p(r) = \frac{d\ln S^A_p(r)}{d\ln r}, \tag{43}$$

$$\mu^A_p(r) = \frac{d\ln Q^A_p(r)}{d\ln r}, \tag{44}$$

where A denotes any of the above quantities.

Since we are interested in the scaling behavior in the inertial-convective range at high Reynolds number which is expected to be insensitive to the dissipation range [36], we examine the curves of the local scaling exponents for run C at the highest Reynolds number in the present study. The results for other runs are qualitatively the same. Figure 12 compares the local scaling exponents as functions of r for the order $p = 4$, 6, and 8 for run C. The general trend of the curves is that when r/η increases from the dissipation range, the curves decrease from values close to the analytical value p for pth-order moments, becoming nearly horizontal at around $r/\eta \approx 100$, thus signifying power-law scaling; finally, decay occurs at large separation distances. Further examination shows that (1) the width of the horizontal portion becomes wider approximately in the order of $\delta_r u^L$, $\delta_r u^T$, $\delta_r w^L$, and $\delta_r w^T$, and (2) the crossover length $r^{A,L}_{*,p}$ is defined as the length scale at the low end of

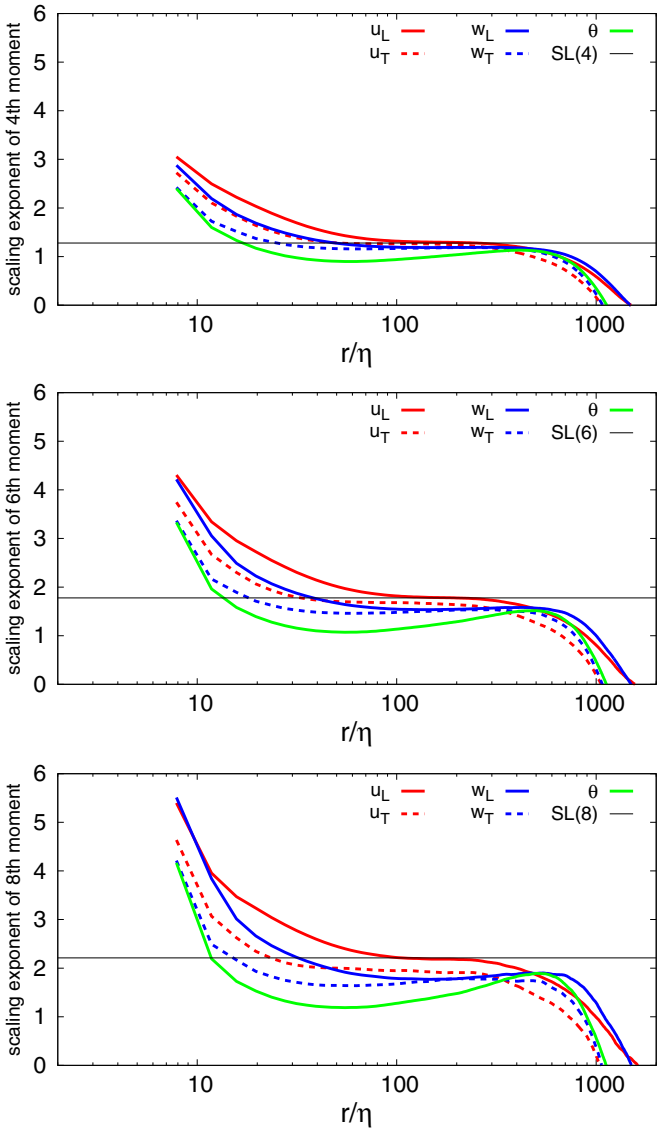

FIG. 12. Comparison of local scaling exponents for run C: top, fourth order; middle, sixth order; bottom, eighth order. Horizontal line with $SL(p)$ shows the exponents according to the She-Lévêque model [55].

the horizontal part of the curve. Then, $r_{*,p}^{A,T} < r_{*,p}^{A,L}$ for $A = u$ or w and $r_{*,p}^{w,B} < r_{*,p}^{u,B}$ for $B = L$ or T [33], and (3) in the curve for the local scaling exponents of the passive scalar, the horizontal parts are not observed and the curves attain a local minimum at around $r/\eta \approx 60$, linearly increase with $\log(r/\eta)$ in the range $70 < r/\eta < 300$, and reach local maxima at around $r/\eta \approx 600$, as reported in Refs. [13,24]. (4) The local scaling exponents $\xi_p^{w,L}$ and $\xi_p^{w,T}$ at $p = 8$ behave similarly to ξ_p^{θ} for the passive scalar, which suggests that the scaling exponents of the passive vector at high order are not universal [24].

The local scaling exponents of the transfer fluxes $\mu_p^A(r)$ for run C are compared in Fig. 13. All curves decay from their analytical values at small r/η, nearly plateau over the inertial-convective range separation distance, and finally reach zero as r/η increases further.

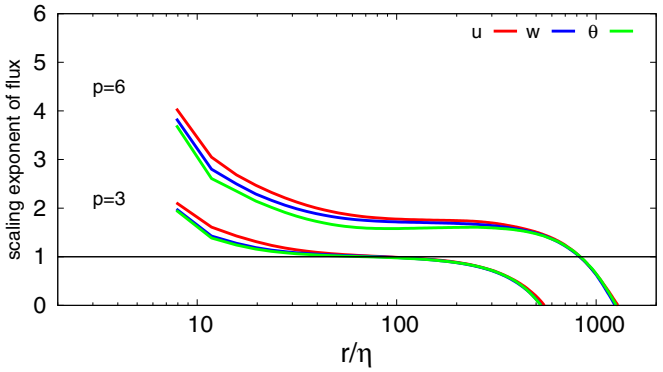

FIG. 13. Comparison of local scaling exponents for fluxes of velocity, passive vector, and passive scalar for run C.

Since the Reynolds numbers in the present DNSs are not high enough and the plateau width of the curves is rather short, it is difficult to compute the scaling exponents in the inertial-convective range. In this circumstance, we evaluate the mean, standard deviation, and maximum and minimum values of the local scaling exponent for each curve as follows. First we examine the local slope of the $\xi_4^A(r)$ curve by computing $s_4^A(r) = d\xi_4^A(r)/d\ln r$ for $A = u, w, \theta$ and identify the range of scale r/η satisfying the condition $|s_4^A(r)| < 0.1$, say, $r_{\min} < r < r_{\max}$. Within this range, we computed the mean value of $\overline{\xi}_p^A$ and the minimum value $\xi_{p,\min}^A$ and the maximum value $\xi_{p,\max}^A$. When the condition $|s_4^A(r)| < 0.1$ is not satisfied, the exponents are not computed. The mean values of the scaling exponents with error bars (in terms of the maximum and minimum values) are plotted as functions of the order p in Fig. 14 for ξ_p^A (top) and for μ_p^A (bottom), respectively [15,24,33,55]. Also the scaling exponents for all runs are summarized in Table II. It is found that $\xi_p^\theta < \xi_p^{wT} < \xi_p^{wL} < \xi_p^{uT} < \xi_p^{uL}$ for $p > 4$. If it is measured in terms of the scaling exponents, the intermittency intensity of the passive vector is intermediate between the velocity and passive scalar. The μ_p^w is slightly smaller than, but close to, μ_p^u, and larger than μ_p^θ. Again, the value is intermediate between the velocity and passive scalar.

F. Effects of Reynolds number and forcing method

The effects of the Reynolds number and large-scale forcing on the scaling exponents can be examined by comparing the values in Table II. The effects of the Reynolds number are seen by comparing runs A, B, and C for the same forcing, while the large-scale forcing effects are found by comparing runs B and D at a fixed Reynolds number. Although the Reynolds numbers in the present computations are not large enough to fully determine the trend and the scaling exponents are slightly scattered, the general trend is that the scaling exponents of the passive vector at low to moderate order are insensitive to variation in the Reynolds numbers and the large-scale forcing in the present study.

V. SUMMARY

To explore the physical mechanism that causes similarities and differences in statistical properties between the velocity and passive scalar fluctuations, we introduced an incompressible passive vector $\boldsymbol{w}$ accompanied by the pseudopressure which shares as many common properties and structure as both of the Navier-Stokes and passive scalar equations. The statistical properties of the passive vector have been examined in comparison with those of the velocity and passive

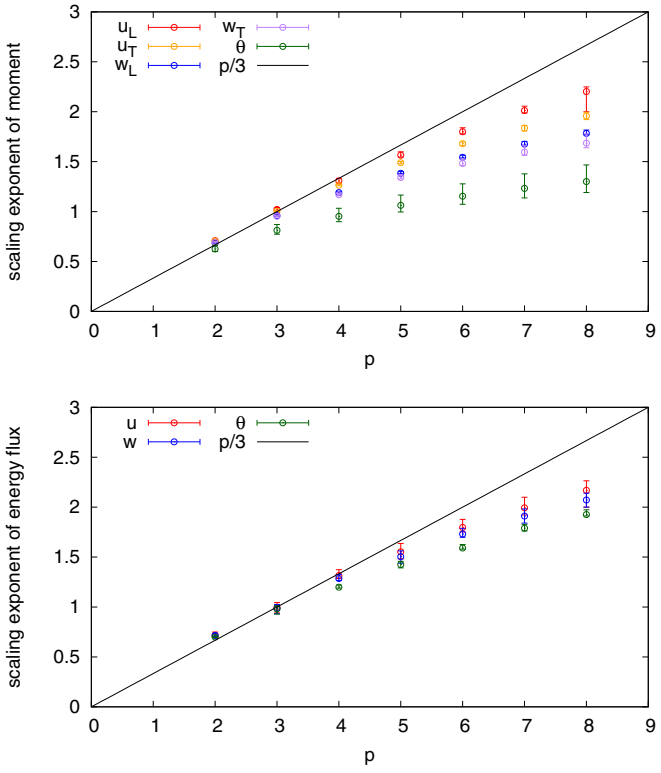

FIG. 14. Variation of scaling exponents of moments of increments (top) and transfer fluxes (bottom) over p for run C.

scalar, especially focusing on the high-order statistics for various Reynolds numbers and different large-scale forcings.

The following properties are observed: (1) $P(w)$ is wider than $P(u)$, while $P(\theta)$ is narrower than the two PDFs, and (2) $P(\log_{10}(\epsilon_w/\bar{\epsilon}_w))$ and $P(\log_{10}(\epsilon_u/\bar{\epsilon}_u))$ are close to each other and almost log-normal distribution, while $P(\log_{10}(\epsilon_\theta/\bar{\epsilon}_\theta))$ has a long tail on the negative side and decays faster than the log-normal distribution on the positive side.

The most striking differences between the incompressible velocity and passive vector are found in the visualized field and the PDFs of the pressure and pseudopressure. The visualization of the three fields showed that the pseudoenstrophy Ω_w is roughly sheetlike, similar to Ω_θ for the passive scalar, while the enstrophy is tubelike. Unlike the pressure PDF, which is negatively skewed, the PDF $P(q)$ has long tails on both sides and is closer to symmetry than the pressure PDF which can be understood in relation to the sheetlike structure of Ω_w.

The local scaling exponents for the velocity are consistent with those in the previous studies and those of the passive scalar are found to slowly increase as the separation distance increases, as found in Ref. [24]. The local scaling exponents of the moments $\langle|\delta w_{L,T}(r)|^p\rangle$ for $p = 4, 6$ have approximate plateaus in the inertial convective range; however, the local scaling exponents at high order $p = 8$ behave similarly to that of the passive scalar. The scaling exponents of the passive vector are anomalous, intermediate between those of the velocity and passive scalar, and the high-order exponents are nonuniversal, unlike the normal scaling of the passive vector for the Kraichnan velocity ensemble as shown by Adzhemyan and Antonov [27]. The crossover length $r_{*,p}^{w,B}$ for $B = L$ or T from the dissipation to the inertial range for the passive vector is examined; it was found that $r_{*,p}^{w,T} < r_{*,p}^{w,L}$ for $p = 4, 6, 8$ which is again similar to the case of the velocity. The scaling exponents

TABLE II. Scaling exponents of moments of increments and transfer fluxes in the inertial-convective range. Mean, standard deviation, maximum, and minimum values are computed in the range $[r_{\min}/\eta, r_{\max}/\eta]$ in which the absolute value of the local slope is smaller than 0.1 (see more in the text). For run A, ξ_p^{Lu} and μ_p^A are not computed because of short range.

		Run A				Run B				Run C				Run D			
	Range/p	Mean	Std	Min	Max	Mean	Std	Min	Max	Mean	Std	Min	Max	Mean	Std	Min	Max
ξ_p^{uL}	Range						[80,233]				[82,310]				[85,199]		
	4					1.28	0.02	1.24	1.33	1.30	0.02	1.25	1.34	1.26	0.03	1.21	1.30
	6					1.76	0.04	1.69	1.83	1.79	0.03	1.72	1.85	1.72	0.04	1.64	1.79
	8					2.15	0.05	2.00	2.24	2.19	0.03	2.00	2.26	2.08	0.06	1.99	2.18
ξ_p^{uT}	Range		[56,126]				[52,159]				[55,204]				[52,120]		
	4	1.21	0.00	1.21	1.22	1.24	0.01	1.22	1.25	1.26	0.01	1.24	1.27	1.23	0.01	1.21	1.25
	6	1.60	0.03	1.57	1.65	1.64	0.00	1.62	1.65	1.67	0.02	1.64	1.70	1.64	0.02	1.60	1.66
	8	1.88	0.07	1.79	2.01	1.92	0.01	1.89	1.93	1.95	0.03	1.91	1.99	1.91	0.03	1.86	1.94
ξ_p^{wL}	Range		[70,146]				[74,307]				[78,424]				[80,217]		
	4	1.22	0.01	1.20	1.23	1.19	0.01	1.17	1.21	1.19	0.01	1.18	1.21	1.19	0.02	1.17	1.22
	6	1.60	0.00	1.60	1.61	1.55	0.02	1.53	1.58	1.55	0.01	1.54	1.58	1.57	0.02	1.53	1.61
	8	1.88	0.03	1.85	1.92	1.79	0.03	1.76	1.86	1.81	0.04	1.77	1.89	1.81	0.03	1.78	1.87
ξ_p^{wT}	range		[36,125]				[41,239]				[43,350]				[46,191]		
	4	1.20	0.01	1.19	1.21	1.17	0.01	1.16	1.18	1.17	0.01	1.16	1.19	1.14	0.01	1.12	1.16
	6	1.54	0.03	1.51	1.58	1.49	0.01	1.47	1.51	1.50	0.03	1.46	1.54	1.44	0.01	1.43	1.46
	8	1.77	0.06	1.71	1.90	1.68	0.02	1.65	1.73	1.71	0.06	1.64	1.79	1.59	0.05	1.53	1.69
ξ_p^{θ}	Range		[47,146]				[54,294]				[59, 412]				[57,196]		
	4	1.03	0.05	0.96	1.11	1.00	0.07	0.90	1.10	1.01	0.08	0.90	1.13	0.94	0.03	0.90	0.98
	6	1.29	0.09	1.17	1.45	1.23	0.11	1.09	1.42	1.25	0.13	1.07	1.50	1.15	0.04	1.09	1.21
	8	1.50	0.13	1.33	1.73	1.41	0.14	1.22	1.68	1.44	0.20	1.19	1.84	1.29	0.05	1.23	1.36
	Range						[52,186]				[47,275]				[54,165]		
μ_p^u	3					0.94	0.07	0.79	1.04	0.97	0.07	0.80	1.06	0.95	0.06	0.83	1.03
	6					1.77	0.04	1.70	1.86	1.79	0.06	1.72	1.93	1.75	0.05	1.67	1.85
μ_p^w	3					0.95	0.06	0.81	1.02	0.96	0.07	0.79	1.04	0.94	0.05	0.83	1.01
	6					1.72	0.03	1.66	1.79	1.72	0.04	1.66	1.83	1.72	0.04	1.66	1.79
μ_p^{θ}	3					0.93	0.06	0.78	1.00	0.95	0.06	0.79	1.02	0.94	0.05	0.83	1.00
	6					1.58	0.01	1.56	1.62	1.60	0.02	1.58	1.67	1.54	0.03	1.49	1.60

of the passive vector moments and transfer fluxes are found to be between the velocity and passive scalar for the order $p \geqslant 4$. As argued in Ref. [25], the pseudopressure behaves similarly to the pressure at large scales, while its role is secondary at small scales. At small scales, the difference between the velocity and passive vector manifests in the dynamics, i.e., whether they are linear or nonlinear, and the nonlinearity dominates the small-scale (or local) structure of the flow field, such as the vortex tube or sheet [56,57]. The sheetlike structure of the passive vector $\boldsymbol{w}$ resembles the sheetlike structure of the current sheet in a magnetic field [58,59]. Although there are differences in dynamics among the three passive fields, incompressible passive vector $\boldsymbol{w}$, incompressible passive magnetic field $\boldsymbol{B}$, and the passive scalar θ, a common feature in the above findings is the linearity of the fundamental equations. In contrast, the Navier-Stokes equation is nonlinear, so the vortex tube is formed through Kelvin-Helmholtz instability.

Based on the above arguments, we conclude that the scaling exponents of the passive vector are anomalous and nonuniversal at high order, and the strength of the intermittency is intermediate between the velocity and passive scalar, and that the linearity of the fundamental equation tends to lead to stronger intermittency.

ACKNOWLEDGMENTS

The National Institute for Fusion Science, Japan (Grants No. NIFS16KNSS076 and No. NIFS18KNSS105) is gratefully acknowledged for providing computational resources. The Networking, Large-scale Data Analyzing and Information Systems (JHPCN) (Grants No. jh180009 and No. jh190018) and High Performance Computing (HPC2018) at Nagoya University, and ES at JAMSTEC are also acknowledged. The work of T.G. was supported by MEXT KAKENHI through Grant No. 15H02218, and JSPS KAKENHI Grants No. 17K05734 for H.M. and No. 18K03925 for T.W. are highly appreciated.

[1] A. N. Kolmogorov, The local structure of turbulence in an incompressible fluid for very large Reynolds numbers, Dokl. Akad. Nauk. SSSR **30**, 301 (1941).

[2] A. M. Obukhov, Structure of the temperature field in a turbulent flow, Izv. Akad. Nauk. SSSR, Ser. Geogr. Geofiz. **13**, 58 (1949).

[3] A. M. Yaglom, Local structure of the temperature field in a turbulent flow, Dokl. Akad. Nauk. SSSR **69**, 743 (1949).

[4] S. Corrsin, On the spectrum of isotropic temperature fluctuations in isotropic turbulence, J. Appl. Phys. **22**, 469 (1951).

[5] G. K. Batchelor, Small-scale variation of convected quantities like temperature in turbulent fluid. Part 1. General discussion and the case of small conductivity, J. Fluid Mech. **5**, 113 (1959).

[6] G. K. Batchelor, I. K. Howells, and A. A. Townsend, Small-scale variations of convected quantities like temperature in turbulent fluid, Part 2: The case of large conductivity, J. Fluid Mech. **5**, 134 (1959).

[7] A. S. Monin and A. M. Yaglom, *Statistical Fluid Mechanics: Mechanics of Turbulence* (MIT Press, Cambridge, MA, 1975), Vol. 2.

[8] U. Frisch, *Turbulence: The Legacy of A. N. Kolmogorov* (Cambridge University Press, Cambridge, UK, 1995).

[9] T. Ishihara, T. Gotoh, and Y. Kaneda, Study of high-Reynolds number isotropic turbulence by direct numerical simulation, Ann. Rev. Fluid Mech. **41**, 165 (2009).

[10] T. Gotoh and P. K. Yeung, Passive scalar transport in turbulence, a computational perspective, in *Ten Chapters in Turbulence*, edited by P. Davidson, Y. Kaneda, and K. R. Sreenivasan (Cambridge University Press, Cambridge, UK, 2013).

[11] R. A. Antonia, E. J. Hopfinger, Y. Gagne, and F. Anselmet, Temperature structure functions in turbulent shear flows, Phys. Rev. A **30**, 2704 (1998).

[12] F. Moisy, H. Willaime, J. S. Andersen, and P. Tabeling, Passive Scalar Intermittency in Low Temperature Helium Flows, Phys. Rev. Lett. **86**, 4827 (2001).

[13] T. Watanabe and T. Gotoh, Statistics of a passive scalar in homogeneous turbulence, New J. Phys. **6**, 40 (2004).

[14] T. Watanabe and T. Gotoh, Intermittency in passive scalar turbulence under the uniform mean scalar gradient, Phys. Fluids **18**, 058105 (2006).

[15] E. W. Saw, P. Debue, D. Kuzzay, F. Daviaud, and B. Dubrulle, On the universality of anomalous scaling exponents of structure functions in turbulent flows, J. Fluid Mech. **837**, 657 (2018).

[16] R. H. Kraichnan, Small scale structure of a scalar field convected by turbulence, Phys. Fluids **11**, 945 (1968).

[17] R. H. Kraichnan, Anomalous Scaling of a Randomly Advected Passive Scalar, Phys. Rev. Lett. **72**, 1016 (1994).

[18] K. Gawedzki and A. Kupiainen, Anomalous Scaling of the Passive Scalar, Phys. Rev. Lett. **75**, 3834 (1995).

[19] M. Vergassola, Anomalous scaling for passively advected magnetic fields: Passive scalar intermittency in low temperature helium flows, Phys. Rev. E **53**, R3021(R) (1996).

[20] A. Celani, A. Lanotte, A. Mazzino, and M. Vergassola, Universality and Saturation of Intermittency in Passive Scalar Turbulence, Phys. Rev. Lett. **84**, 2385 (2000).
[21] A. Celani, A. Lanotte, A. Mazzino, and M. Vergassola, Fronts in passive scalar turbulence, Phys. Fluids **13**, 1768 (2001).
[22] K. Gawedzki and M. Vergassola, Phase transition in the passive scalar advection, Phys. D (Amsterdam, Neth.) **138**, 63 (2000).
[23] G. Falkovich, K. Gawedzki, and M. Vergassola, Particles and fields in fluid turbulence, Rev. Mod. Phys. **73**, 913 (2001).
[24] T. Gotoh and T. Watanabe, Power and Non-power Laws of Passive Scalar Moments Convected by Isotropic Turbulence, Phys. Rev. Lett. **115**, 114502 (2015).
[25] J. Yang, T. Gotoh, and H. Miura, Statistical properties of incompressible passive vector convected by isotropic turbulence, Phys. Rev. Fluids **4**, 064601 (2019).
[26] K. Yoshida and Y. Kaneda, Anomalous scaling of anisotropy of second-order moments in a model of a randomly advected solenoidal vector field, Phys. Rev. E **63**, 016308 (2000).
[27] L. Ts. Adzhemyan, N. V. Antonov, A. Mazzino, P. Muratore-Ginanneschi, and A. V. Runov, Pressure and intermittency in passive vector turbulence, Europhys. Lett. **55**, 801 (2001).
[28] R. Benzi, L. Biferale, and F. Toschi, Universality in passively advected hydrodynamic fields: The case of a passive vector with pressure, Eur. Phys. J. B **24**, 125 (2001).
[29] E. S. C. Ching, Y. Cohen, T. Gilbert, and I. Procaccia, Active and passive fields in turbulent transport: The role of statistically preserved structures, Phys. Rev. E **67**, 016304 (2003).
[30] N. V. Antonov, M. Hnatich, J. Honkonen, and M. Jurčišin, Turbulence with pressure: Anomalous scaling of a passive vector field, Phys. Rev. E **68**, 046306 (2003).
[31] H. Arponen, Steady-state existence of passive vector fields under the Kraichnan model, Phys. Rev. E **81**, 036325 (2010).
[32] N. V. Antonov and N. M. Gulitskiy, Anisotropic turbulent advection of a passive vector field: Effects of the finite correlation time, EPJ Web Conf. **108**, 02008 (2016).
[33] T. Gotoh, D. Fukayama, and T. Nakano, Velocity field statistics in homogeneous steady turbulence obtained using a high-resolution direct numerical simulation, Phys. Fluids **14**, 1065 (2002).
[34] D. A. Donzis and P. K. Yeung, Resolution effects and scaling in numerical simulations of passive scalar mixing in turbulence, Phys. D (Amsterdam, Neth.) **239**, 1278 (2010).
[35] T. Gotoh, S. Hatanaka, and H. Miura, Spectral compact difference hybrid computation of passive scalar in isotropic turbulence, J. Comput. Phys. **231**, 7398 (2012).
[36] T. Watanabe and T. Gotoh, Inertial-range intermittency and accuracy of direct numerical simulation for turbulence and passive scalar turbulence, J. Fluid Mech. **590**, 117 (2007).
[37] T. Ishihara, K. Morishita, M. Yokokawa, A. Uno, and Y. Kaneda, Energy spectrum in high-resolution direct numerical simulations of turbulence, Phys. Rev. Fluids **1**082403(R) (2016).
[38] Y. Kaneda, T. Ishihara, M. Yokokawa, K. Itakura, and A. Uno, Energy dissipation rate and energy spectrum in high resolution direct numerical simulations of turbulence in a periodic box, Phys. Fluids **15**, L21 (2003).
[39] D. A. Donzis and K. R. Sreenivasan, The bottleneck effect and the Kolmogorov constant in isotropic turbulence, J. Fluid Mech. **657**, 171 (2010).
[40] J. Jiménez, A. A. Wray, P. G. Saffman, and R. S. Rogallo, The structure of intense vorticity in isotropic turbulence, J. Fluid Mech. **255**, 65 (1993).
[41] R. Prasad and K. R. Sreenivasan, Quantitative three-dimensional imaging and the structure of passive scalar fields in fully turbulent flows, J. Fluid Mech. **216**, 1 (1990).
[42] K. A. Buch and W. J. A. Dahm, Experimental study of the fine-scale structure of conserved scalar mixing in turbulent shear flows. Part 1. Sc $\gg$ 1, J. Fluid Mech. **317**, 21 (1996).
[43] T. Gotoh, T. Watanabe, and H. Miura, Spectrum of passive scalar at very high Schmidt number in turbulence, Plasma Fusion Res. **9**, 3401019 (2014).
[44] Jayesh and Z. Warhaft, Probability Distribution of a Passive Scalar in Grid-Generated Turbulence, Phys. Rev. Lett. **67**, 3503 (1991).

[45] Jayesh and Z. Warhaft, Probability distribution, conditional dissipation, and transport of passive temperature fluctuations in grid-generated turbulence, Phys. Fluids A **4**, 2292 (1992).
[46] E. S. C. Ching and Y. Tu, Passive scalar fluctuations with and without a mean gradient: A numerical study, Phys. Rev. E **49**, 1278 (1994).
[47] A. Bourlioux and A. J. Majda, Elementary models with probability distribution function intermittency for passive scalars with a mean gradient, Phys. Fluids **14**, 881 (2002).
[48] N. Cao, S. Chen, and G. D. Doolen, Statistics and structures of pressure in isotropic turbulence, Phys. Fluids **11**, 2235 (1999).
[49] T. Gotoh and R. S. Rogallo, Intermittency and scaling of pressure at small scales in forced isotropic turbulence, J. Fluid Mech. **396**, 257 (1999).
[50] T. Gotoh and T. Watanabe, Scalar flux in a uniform mean scalar gradient in homogeneous isotropic steady turbulence, Phys. D (Amsterdam, Neth.) **241**, 141 (2012).
[51] T. Gotoh and R. H. Kraichnan, Turbulence and Tsallis statistics, Phys. D (Amsterdam, Neth.) **193**, 231 (2004).
[52] A. N. Kolmogorov, A refinement of previous hypotheses concerning the local structure of turbulence in a viscous incompressible fluid at high Reynolds number, J. Fluid Mech. **13**, 82 (1962).
[53] P. K. Yeung, D. A. Donzis, and K. R. Sreenivasan, Dissipation, enstrophy and pressure statistics in turbulence simulations at high Reynolds numbers, J. Fluid Mech. **700**, 5 (2012).
[54] D. Buaria, A. Pumir, E. Bordenschatz, and P. K. Yeung, Extreme velocity gradients in turbulent flows, New J. Phys. **21**, 043004 (2019).
[55] Z.-S. She and E. Lévêque, Universal Scaling Laws in Fully Developed Turbulence, Phys. Rev. Lett. **72**, 336 (1994).
[56] R. H. Kraichnan, Turbulent cascade and intermittency growth, Proc. R. Soc. London A **434**, 65 (1991).
[57] T. Gotoh and T. Nakano, Role of pressure in turbulence, J. Stat. Phys. **113**, 855 (2003).
[58] D. Hori and H. Miura, Spectrum properties of Hall MHD turbulence, Plasma Fusion Res. **3**, S1053 (2008).
[59] H. Miura and K. Araki, Structure transitions induced by the Hall term in homogeneous and isotropic magnetohydrodynamic turbulence, Phys. Plasmas **21**, 072313 (2014).